Modeling and Identification of Coupled Translational and Rotational Motion of Underactuated Indoor Miniature Autonomous Blimps

Qiuyang Tao, Mengxue Hou, and Fumin Zhang

Abstract— Swing oscillation is widely observed among indoor miniature autonomous blimps (MABs) due to their underactuated design and unique aerodynamic shape. A detailed dynamics model is critical for investigating this undesired movement and designing controllers to stabilize the oscillation. This paper presents a motion model that describes the coupled translational and rotational movements of a typical indoor MAB with saucer-shaped envelope. The kinematics and dynamic model of the MAB are simplified from the six-degrees-of-freedom (6-DOF) Newton–Euler equations of underwater vehicles. The model is then reduced to 3-DOF given the symmetrical design of the MAB around its vertical axis. Parameters of the motion model are estimated from the system identification experiments, and validated with experimental data.

Fig. 1. Photo of the indoor miniature blimp GT-MAB.

I. INTRODUCTION

Indoor aerial robots are gaining increasing attention owing to their promising applications including surveillance, building exploration, human-robot interaction (HRI), and search and rescue [1]–[4]. However, most existing indoor aerial platforms, such as quadcopters, have fast-spinning propellers which may cause safety concerns in human-occupied indoor environments [5]–[7]. Besides, these platforms usually have limited flight endurance [4], [8], typically less than 10 minutes for nano drones [9], which restricts their applications.

We develop the Georgia-Tech Miniature Autonomous Blimp (GT-MAB), a lighter-than-air robot specifically designed for indoor applications [10]. The diameter of GT-MAB is only around 0.7 meters, which ensures the agility in confined indoor space. Despite the miniature size, GT-MAB features omnidirectional actuation, and payload capacity that can carry a wide range of onboard sensors [11]. As shown in Fig. 1, GT-MAB has ducted main thrusters and is cushioned with a helium-filled envelope, which makes the robot safe to fly indoors, causing no threat to human and the surroundings even when collision happens. With the lifting force provided by buoyancy, GT-MAB has loiter time for more than 2 hours [12]. The extended flight endurance makes GT-MAB well-suited to many applications that require sustained airborne presence [13].

We design the flight controller of GT-MAB by decomposing its movement into a set of motion primitives [12]. This decoupled modeling and control approach has successfully supported many applications of GT-MAB including 3D field mapping [12], [14], human-robot interaction [11], [15], and testbed for deep-learning-based localization and multi-agent path planning [16], [17]. However, lateral and longitudinal

oscillation is often observed due to the underactuated design and the unique aerodynamic shape of GT-MAB. This undesirable oscillation could cause inaccurate sensor readings, unstable video streams from the onboard camera, and less comfortable HRI experience. Our recent works [18], [19] identified the rotational motion of GT-MAB and designed a control system to stabilize the swing oscillation during hovering flight. However, the control system introduced in [18] cannot stabilize the oscillation in cruising flight. The dynamics of the swing motion becomes significantly more complicated for cruising, since there is a strong coupling between the translational and rotational motion.

The unique aerodynamic shape, the non-smooth envelope, and the slow-flying nature of indoor blimps are the major difficulties in modeling the motion of GT-MAB. In contrast to outdoor airships with cigar-shaped envelope, GT-MAB has a "saucer-shaped" envelope for omnidirectional maneuverability and adequate buoyancy with smaller footprint. Also, due to the high agility and safety requirements for indoor operation, there is no trail fin or control surface on GT-MAB. As a result, analytical methods for modeling outdoor airships such as [20], [21] cannot be applied. Indoor blimps usually use Mylar film for lower gas permeability [22]. However, as seen in Fig. 1, folding is usually inevitable on this non-stretchable envelope. The imperfect shape may cause inaccuracy when calculating model parameters from the geometry of the blimp [23]. The complex geometry of the non-smooth envelope also makes it hard to estimate model parameters with CFD (computational fluid dynamics) simulations like [24]. Moreover, wind tunnel experiments for outdoor airships like [25], [26] cannot be conducted on the slow-flying indoor MABs since the tests are usually designed for high-speed vehicles.

The authors are with the School of Electrical and Computer Engineering, Georgia Institute of Technology, Atlanta, GA 30332, USA {qiuyang,mhou30,fumin}@gatech.edu

The existing approaches for modeling the dynamics of indoor miniature blimps can be categorized into two groups, analytical and data-driven. The analytical methods investigate the aerodynamics from the specific shape of the blimp [27]. [28] presented the 6-DOF motion model of a cigar-shaped indoor blimp. The model was then simplified to only containing the decoupled movements on the horizontal plane for the convenience of studying the control strategy under wind disturbance. [29] established the 6-DOF mathematical model of a cigar-shaped indoor blimp. The model was then simplified by removing the dynamics of the roll and pitch motion. [27] also presented the 6-DOF model of a cigar-shaped indoor blimp. The model parameters were analytically derived from the geometry of the envelope. Pragmatic experiments were also introduced to evaluate the damping coefficients. Unfortunately, analytical methods may only be valid for a specific class of envelope shapes [24]. As a result, existing analytical methods on determining model parameters for traditional cigar-shaped blimps cannot be applied to saucer-shaped GT-MAB. Data-driven approaches identify the model parameters of MABs from measurements. [30] established the 1-DOF motion model of an indoor blimp for altitude control, and identified the parameters from the height measurement under step input. Our previous work [12] simplified the motion model of GT-MAB into decoupled translational and steering movements, and each motion primitive was identified separately. The recent work [31] simplified the 6-DOF model of an indoor blimp as decoupled altitude and planar movements. However, the roll and pitch motions were not considered in both works [12], [31]. Our recent works [18], [19] investigated the swing oscillation of indoor blimps by modeling and identifying the rotational motion of GT-MAB. [32] established the 6-DOF motion model of an indoor MAB, and introduced the experiment for identifying the translational drag coefficients.

In this paper, we extend our previous efforts on modeling the swing motion of GT-MAB by including the coupling between the translational and rotational movements into consideration. We incorporate the generic kinematics and dynamic model of underwater vehicles given that the density of GT-MAB is identical to the surrounding fluid. The 6-DOF motion model of GT-MAB is derived based on its mechanical design. The full model is then reduced to 3-DOF given the symmetry of GT-MAB around its vertical axis. Parameters of the simplified model are identified and verified with experimental data. The swing oscillation is a common problem among indoor miniature blimps. Finless bottom-heavy underactuated design is widely adopted by many indoor MABs such as [22], [33]. Therefore, the proposed methods in this paper could be applied to other indoor miniature blimps.

This paper is organized as follows: in Section II, we establish the 6-DOF motion model of GT-MAB. In Section III, the model is reduced to 3-DOF given the symmetric design of the blimp. In Section IV, we identify and validate the parameters of the simplified model. In Section V, we draw conclusion and discuss future work.

II. MOTION MODEL FOR GT-MAB

In this section, we establish the dynamic model of the miniature indoor blimp, GT-MAB, driven by the gondola-mounted thrusters located underneath the symmetric saucer-shaped envelope.

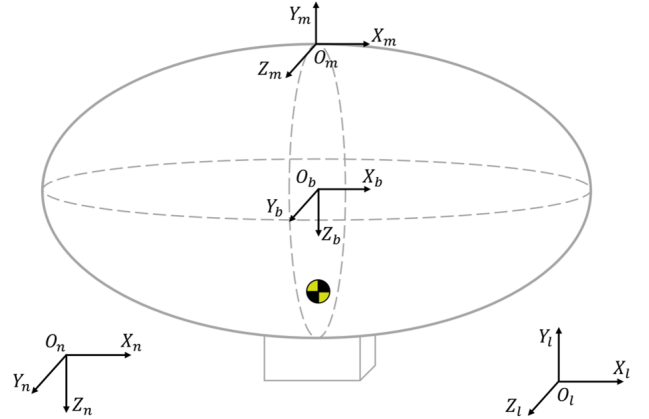### A. Coordinate Frames and Kinematics

Fig. 2.   Illustration of the coordinate frames.

Fig. 2 shows the definition of the inertial frame, the coordinates of the motion capture system, and the body-fixed frames that separately attached at the center of buoyancy (CB) and the localization markers. The inertial frame is denoted by $\{n\}$ with north-east-down (NED) convention. Given the fact that indoor blimps always operate in confined environments at low speed, we apply flat-earth approximation and neglect the movement of the earth. Positioning devices usually have different coordinate systems other than $\{n\}$. Therefore $\{l\}$ is defined to represent the frames used in the motion capture system. The definition of $\{l\}$ will help convert the pose of the blimp to $\{n\}$. Given that most localization devices have fixed installation, we assume $\{l\}$ is also earth-fixed. In this paper, we use the OptiTrack system with Y-up convention. For simplicity, O_n is defined at the same position as O_l, and the x-axes of both frames are aligned. The body frame $\{b\}$ is established at the CB of GT-MAB, which is the geometric center of the envelope. The localization markers are installed at the top of the envelope for the best visibility to the ceiling-mounted motion tracking system. The frame attached at the marker position is denoted as $\{m\}$. The marker frame has the same Y-up convention as $\{l\}$ for the convenience of pose calibration in the motion capture system.

The pose of GT-MAB is denoted as $\boldsymbol{\eta}_{b/n}^n = [\boldsymbol{p}_{b/n}^{n\top}, \boldsymbol{\Theta}_{nb}^\top]^\top$, which is the pose of $\{b\}$ with respect to $\{n\}$ expressed in the inertial frame. $\boldsymbol{p}_{b/n}^n \in \mathbb{R}^3$ and $\boldsymbol{\Theta}_{nb} \in \mathbb{S}^3$ represent the position and orientation separately. The instantaneous velocity of the blimp decomposed in the body frame $\{b\}$ is described by $\boldsymbol{\nu}_{b/n}^b = [\boldsymbol{v}_{b/n}^{b\top}, \boldsymbol{\omega}_{b/n}^{b\top}]^\top$, where $\boldsymbol{v}_{b/n}^b \in \mathbb{R}^3$ and $\boldsymbol{\omega}_{b/n}^b \in \mathbb{R}^3$ are the linear and angular velocities. From [34], the relationship

340

between $\boldsymbol{\nu}_{b/n}^b$ and the rate of change of $\boldsymbol{\eta}_{b/n}^n$ is given by:

$$\dot{\boldsymbol{\eta}}_{b/n}^n = \begin{bmatrix} \dot{\boldsymbol{p}}_{b/n}^n \\ \dot{\boldsymbol{\Theta}}_{nb} \end{bmatrix} = \begin{bmatrix} \boldsymbol{R}_b^n(\boldsymbol{\Theta}_{nb}) & \boldsymbol{0}_{3\times3} \\ \boldsymbol{0}_{3\times3} & \boldsymbol{T}_\Theta(\boldsymbol{\Theta}_{nb}) \end{bmatrix} \begin{bmatrix} \boldsymbol{v}_{b/n}^b \\ \boldsymbol{\omega}_{b/n}^b \end{bmatrix} \quad (1)$$
$$= \boldsymbol{J}_\Theta(\boldsymbol{\eta}_{b/n}^n)\boldsymbol{\nu}_{b/n}^b,$$

where $\boldsymbol{R}_b^n(\boldsymbol{\Theta}_{nb})$ is the rotation matrix. $\boldsymbol{\Theta}_{nb} = [\phi, \theta, \psi]^\top$, and ϕ, θ, ψ are the Euler angles between $\{b\}$ and $\{n\}$. With the simplified notation $c\cdot = \cos(\cdot)$, $s\cdot = \sin(\cdot)$, and $t\cdot = \tan(\cdot)$, $\boldsymbol{R}_b^n(\boldsymbol{\Theta}_{nb})$ has the form of:

$$\boldsymbol{R}_b^n(\boldsymbol{\Theta}_{nb}) =$$
$$\begin{bmatrix} c\psi c\theta & -s\psi c\phi + c\psi s\theta s\phi & s\psi s\phi + c\psi s\theta c\phi \\ s\psi c\theta & c\psi c\phi + s\psi s\theta s\phi & -c\psi s\phi + s\psi s\theta c\phi \\ -s\theta & c\theta s\phi & c\theta c\phi \end{bmatrix}. \quad (2)$$

The term $\boldsymbol{T}_\Theta(\boldsymbol{\Theta}_{nb})$ in Eq. (1) can be represented as:

$$\boldsymbol{T}_\Theta(\boldsymbol{\Theta}_{nb}) = \begin{bmatrix} 1 & s\phi t\theta & c\phi t\theta \\ 0 & c\phi & -s\phi \\ 0 & s\phi/c\theta & c\phi/c\theta \end{bmatrix}. \quad (3)$$

B. 6-DOF Dynamic Model and Simplification for GT-MAB

Indoor MABs are usually ballasted to the same density as the surrounding fluid to enable altitude control solely with motor thrust. Thus, the volume-to-mass ratio of an indoor blimp is very large compare to other types of aerial robots. As a result, the aerodynamic damping and added mass cannot be neglected. Moreover, there exists restoring torque due to the displacement between CB and the center-of-gravity (CG). Therefore, given the similar operating conditions between MABs and underwater vehicles, the generic 6-DOF motion model from [34] is described as:

$$\boldsymbol{\tau}^b = \boldsymbol{M}^{CB}\dot{\boldsymbol{\nu}}_{b/n}^b + \boldsymbol{C}^{CB}(\boldsymbol{\nu}_{b/n}^b)\boldsymbol{\nu}_{b/n}^b + \boldsymbol{D}^{CB}(\boldsymbol{\nu}_{b/n}^b)\boldsymbol{\nu}_{b/n}^b + \boldsymbol{g}^{CB}(\boldsymbol{\eta}_{b/n}^n). \quad (4)$$

1) Inertia matrix: $\boldsymbol{M}_{6\times6}^{CB}$ is the total inertia matrix at CB:

$$\boldsymbol{M}^{CB} = \boldsymbol{M}_{RB}^{CB} + \boldsymbol{M}_A^{CB}, \quad (5)$$

where $\boldsymbol{M}_{RB}^{CB}$ and $\boldsymbol{M}_A^{CB}$ represent the rigid-body and added inertia matrix. Given that the gondola has neglectable volume and CB is at the center of the symmetric envelope, the added inertia matrix can be simplified with only diagonal terms:

$$\boldsymbol{M}_A^{CB} = \mathrm{diag}(m_{Ax}, m_{Ay}, m_{Az}, I_{Ax}, I_{Ay}, I_{Az}). \quad (6)$$

The rigid-body inertia matrix of GT-MAB is diagonal at CG, which is defined as:

$$\boldsymbol{M}_{RB}^{CG} = \mathrm{diag}(m_{RB}, m_{RB}, m_{RB}, I_{RBx}, I_{RBy}, I_{RBz}), \quad (7)$$

where m_{RB} is the rigid-body mass of GT-MAB. Since $\boldsymbol{M}_{RB}^{CG}$ is defined at CG, it needs to be transformed to CB with the system transformation matrix [34]:

$$\boldsymbol{M}_{RB}^{CB} = \boldsymbol{H}^\top(\boldsymbol{r}_{g/b}^b)\boldsymbol{M}_{RB}^{CG}\boldsymbol{H}(\boldsymbol{r}_{g/b}^b)$$
$$\boldsymbol{H}(\boldsymbol{r}_{g/b}^b) = \begin{bmatrix} \boldsymbol{I}_{3\times3} & \boldsymbol{S}^\top(\boldsymbol{r}_{g/b}^b) \\ \boldsymbol{0}_{3\times3} & \boldsymbol{I}_{3\times3} \end{bmatrix}, \quad (8)$$

where $\boldsymbol{S}(\cdot)$ is the skew-symmetric cross-product operator. $\boldsymbol{r}_{g/b}^b$ is the position of CG in body frame $\{b\}$. Owing to the symmetric design of GT-MAB, $\boldsymbol{r}_{g/b}^b = [0, 0, r_{z,g/b}^b]^\top$. Therefore, the inertial matrix at CB can be derived as:

$$\boldsymbol{M}^{CB} = \boldsymbol{M}_{RB}^{CB} + \boldsymbol{M}_A^{CB} =$$
$$\begin{bmatrix} m_x & 0 & 0 & 0 & m_{RB}r_{z,g/b}^b & 0 \\ 0 & m_y & 0 & -m_{RB}r_{z,g/b}^b & 0 & 0 \\ 0 & 0 & m_z & 0 & 0 & 0 \\ 0 & -m_{RB}r_{z,g/b}^b & 0 & I_x & 0 & 0 \\ m_{RB}r_{z,g/b}^b & 0 & 0 & 0 & I_y & 0 \\ 0 & 0 & 0 & 0 & 0 & I_z \end{bmatrix}$$
$$\quad (9)$$

where the diagonal terms contain both the rigid-body and added-mass components. Thus, $m_i = m_{RB} + m_{Ai}$, $i \in \{x, y, z\}$. $I_i = I_{RBi} + m_{RB}(r_{z,g/b}^b)^2 + I_{Ai}$, $i \in \{x, y\}$; and $I_z = I_{RBz} + I_{Az}$.

2) Coriolis-centripetal matrix: $\boldsymbol{C}_{6\times6}^{CB}$ also contains components from both rigid-body and added inertia. With the operator $\boldsymbol{C}(\boldsymbol{M}, \boldsymbol{\nu})$ defined in [34], $\boldsymbol{C}^{CB}$ can be found as:

$$\boldsymbol{C}^{CB} = \boldsymbol{C}(\boldsymbol{M}_{RB}^{CB}, \boldsymbol{\nu}_{b/n}^b) + \boldsymbol{C}(\boldsymbol{M}_A^{CB}, \boldsymbol{\nu}_{b/n}^b). \quad (10)$$

3) Aerodynamic damping: The aerodynamic damping can be approximated as proportional to the linear and angular velocities for low-speed indoor blimps [26]. Moreover, owing to the symmetric envelopes used in most indoor MABs, the damping matrix is diagonal at CB:

$$\boldsymbol{D}^{CB}(\boldsymbol{\nu}_{b/n}^b) = \mathrm{diag}(D_{vx}^{CB}, D_{vy}^{CB}, D_{vz}^{CB}, D_{\omega x}^{CB}, D_{\omega y}^{CB}, D_{\omega z}^{CB}). \quad (11)$$

4) Restoration torque: Given that CG is below the center of buoyancy, there exists restoring torque that stabilizes the blimp back to the leveled attitude. Denote $\boldsymbol{r}_g^b$ and $\boldsymbol{r}_b^b$ be the position of CG and CB in the body-frame, and $\boldsymbol{f}_g^b = -\boldsymbol{f}_b^b$ be the gravitational and buoyancy force decomposed in $\{b\}$, the restoring torque can be simplified from [34] as:

$$\boldsymbol{g}^{CB}(\boldsymbol{\eta}_{b/n}^n) = -\begin{bmatrix} \boldsymbol{f}_g^b + \boldsymbol{f}_b^b \\ \boldsymbol{r}_g^b \times \boldsymbol{f}_g^b + \boldsymbol{r}_b^b \times \boldsymbol{f}_b^b \end{bmatrix} = -\begin{bmatrix} \boldsymbol{0} \\ \boldsymbol{r}_g^b \times \boldsymbol{f}_g^b \end{bmatrix}. \quad (12)$$

5) Control effort: $\boldsymbol{\tau}^b \in \mathbb{R}^6$ is the summary of all external forces and moments asserted at CB. In this paper, $\boldsymbol{\tau}^b$ is induced by the motor thrust forces:

$$\boldsymbol{\tau}^b = [f_x^b, f_y^b, f_z^b, \tau_x^b, \tau_y^b, \tau_z^b]^\top. \quad (13)$$

C. 3-DOF Model Reduction

Many indoor blimps including GT-MAB, usually have symmetric envelopes around the vertical axes, and capable of pointing the thrust vector omnidirectionally. Therefore, we can approximate the 6-DOF motion of GT-MAB to 3-DOF movement on a vertical plane. As demonstrated in Fig. 3, if the blimp starts from rest at position A, and targets at waypoint B, the ideal trajectory can be contained within a vertical plane that includes both points. For the convenience of parameter identification, we assume there is no initial lateral velocity, and the initial heading of the blimp is aligned

with the inertial frame. Therefore, the 3-DOF motion on the vertical plane can be written as:

$$\dot{\boldsymbol{p}}_{b/n}^n = [\dot{p}_{x,b/n}^n, 0, \dot{p}_{z,b/n}^n]^\top$$
$$\boldsymbol{\Theta}_{nb} = [0, \theta, 0]^\top \qquad (14)$$
$$\boldsymbol{\tau}^b = [f_x^b, 0, f_z^b, 0, \tau_y^b, 0]^\top.$$

With $\boldsymbol{\Theta}_{nb} = [0, \theta, 0]^\top$, Eq. (2) and Eq. (3) can be simplified as:

$$\boldsymbol{R}_b^n(\boldsymbol{\Theta}_{nb}) = \begin{bmatrix} c\theta & 0 & s\theta \\ 0 & 1 & 0 \\ -s\theta & 0 & c\theta \end{bmatrix}, \boldsymbol{T}_\Theta(\boldsymbol{\Theta}_{nb}) = \begin{bmatrix} 1 & 0 & t\theta \\ 0 & 1 & 0 \\ 0 & 0 & 1/c\theta \end{bmatrix}. \qquad (15)$$

Then, the velocities in the body-fixed frame $\{b\}$ are:

$$\boldsymbol{v}_{b/n}^b = \boldsymbol{R}_b^n(\boldsymbol{\Theta}_{nb})^{-1}\boldsymbol{v}_{b/n}^n = [v_{x,b/n}^b, 0, v_{z,b/n}^b]^\top$$
$$\boldsymbol{\omega}_{b/n}^b = \boldsymbol{T}_\Theta(\boldsymbol{\Theta}_{nb})^{-1}\dot{\boldsymbol{\Theta}}_{nb} = [0, \dot{\theta}, 0]^\top. \qquad (16)$$

Therefore, the equations of the simplified 3-DOF movement can be derived from the 6-DOF motion model in Eq. (4) as:

$$f_x^b = (m_{RB} + m_{Ax})\dot{v}_{x,b/n}^b + m_{RB}r_{z,g/b}^b\dot{\omega}_{y,b/n}^b$$
$$+ (m_{RB} + m_{Az})v_{z,b/n}^b\omega_{y,b/n}^b + D_{vx}^{CB}v_{x,b/n}^b$$
$$f_z^b = (m_{RB} + m_{Az})\dot{v}_{z,b/n}^b - m_{RB}r_{z,g/b}^b(\omega_{y,b/n}^b)^2$$
$$- (m_{RB} + m_{Ax})v_{x,b/n}^b\omega_{y,b/n}^b + D_{vz}^{CB}v_{z,b/n}^b$$
$$\tau_y^b = I_y\dot{\omega}_{y,b/n}^b + m_{RB}r_{z,g/b}^b(\dot{v}_{x,b/n}^b + v_{z,b/n}^b\omega_{y,b/n}^b)$$
$$+ (m_{Ax} - m_{Az})v_{x,b/n}^bv_{z,b/n}^b + D_{\omega y}^{CB}\omega_{y,b/n}^b + r_{z,g/b}^bm_{RB}g\sin(\theta). \qquad (17)$$

Due to the underactuated design of most indoor blimps including GT-MAB, $\tau_y^b = r_{z,t/b}^b f_x^b$, where $r_{z,t/b}^b$ is the vertical position of the longitudinal thruster in $\{b\}$.
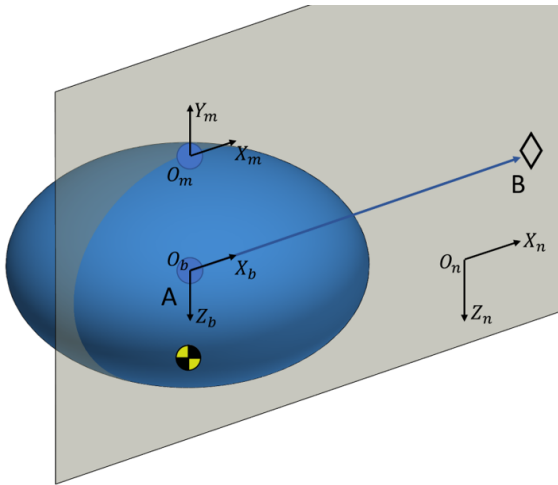

Fig. 3. Motion of GT-MAB reduced to 3-DOF on a vertical plane.

III. PARAMETER IDENTIFICATION

This section identifies the parameters of the motion model described in Eq. (17). Specifically, we aim to find the parameters m_{RB}, m_{Ax}, m_{Az}, I_y, D_{vx}^{CB}, D_{vz}^{CB}, $D_{\omega y}^{CB}$, and $r_{z,g/b}^b$.

A. Data Preparation

Miniature blimps use indoor localization systems due to the GPS-denied environment. These devices usually have different coordinate systems compare to the desired inertial frame. Therefore, measurements from the positioning systems need to be first converted to the inertial frame.

We define the pose of the localization markers measured by the motion capture system as:

$$\boldsymbol{\eta}_{m/l}^l = [\boldsymbol{p}_{m/l}^l, \boldsymbol{\Theta}_{lm}]^\top, \qquad (18)$$

where $\boldsymbol{p}_{m/l}^l$ and $\boldsymbol{\Theta}_{lm}$ represent the position and attitude separately. Next, we calculate the positions of O_m and O_b in the inertial frame as:

$$\boldsymbol{p}_{m/n}^n = \boldsymbol{p}_{l/n}^n + \boldsymbol{R}_l^n(\boldsymbol{\Theta}_{nl})\boldsymbol{p}_{m/l}^l$$
$$\boldsymbol{p}_{b/n}^n = \boldsymbol{p}_{m/n}^n + \boldsymbol{R}_m^n(\boldsymbol{\Theta}_{nm})\boldsymbol{p}_{b/m}^m, \qquad (19)$$

where $\boldsymbol{p}_{l/n}^n$ represents the position of O_l in the inertial frame. In this paper, origins of $\{l\}$ and $\{n\}$ are at the same position. $\boldsymbol{p}_{b/m}^m$ is the position of CB in the body-fixed frame $\{m\}$. For indoor MABs, $\boldsymbol{p}_{b/m}^m$ is usually a constant that solely determined by the geometry of the blimp. $\boldsymbol{\Theta}_{nl}$ and $\boldsymbol{R}_l^n(\boldsymbol{\Theta}_{nl})$ denote the orientation and the corresponding rotation matrix between $\{l\}$ and $\{n\}$. The angles are usually constant due to the fixed installation of the motion capture systems. $\boldsymbol{R}_m^n(\boldsymbol{\Theta}_{nm})$ is the rotation matrix between $\{m\}$ and $\{n\}$, which can be presented as consecutive rotations among $\{n\}$, $\{l\}$ and $\{m\}$:

$$\boldsymbol{R}_m^n(\boldsymbol{\Theta}_{nm}) = \boldsymbol{R}_l^n(\boldsymbol{\Theta}_{nl})\boldsymbol{R}_m^l(\boldsymbol{\Theta}_{lm}). \qquad (20)$$

B. Parameters m_{RB}, m_{Ax}, m_{Az}, D_{vx}^{CB}, and D_{vz}^{CB}

The added mass and aerodynamic damping coefficients of GT-MAB are both diagonal at CB, which characterize the motion along body-frame axes. System identification experiments are designed to estimate these parameters from the motion of GT-MAB along X_b and Z_b axes separately.

In the scenario where the movement of GT-MAB is solely along X_b or Z_b axis, the motion model described in Eq. (17) can be represented as:

$$f_x^b = f_{gx}^b + f_{bx}^b = (m_{RB} + m_{Ax})\dot{v}_{x,b/n}^b + D_{vx}^{CB}v_{x,b/n}^b$$
$$f_z^b = f_{gz}^b + f_{bz}^b = (m_{RB} + m_{Az})\dot{v}_{z,b/n}^b + D_{vz}^{CB}v_{z,b/n}^b. \qquad (21)$$

Furthermore, if the movements in Eq. (21) are both along Z_n, as demonstrated in Fig. 4, we can describe the motion in the inertial frame as:

$$\begin{bmatrix} \dot{p}_{z,b/n}^n \\ \ddot{p}_{z,b/n}^n \end{bmatrix} = \begin{bmatrix} 0 & 1 \\ 0 & -D_{vi}^{CB}/m_i \end{bmatrix} \begin{bmatrix} p_{z,b/n}^n \\ \dot{p}_{z,b/n}^n \end{bmatrix} + \begin{bmatrix} 0 \\ 1/m_i \end{bmatrix}(f_{gz}^n + f_{bz}^n), \qquad (22)$$

where $p_{z,b/n}^n$ is the vertical position of the blimp in $\{n\}$. $m_i = m_{RB} + m_{Ai}$, $i \in \{x, z\}$. f_{gz}^n and f_{bz}^n are the total gravitational and buoyancy forces expressed in the inertial frame.

As illustrated in Fig. 4, system identification experiments are designed to create the motion solely along X_b or Z_b axis. We adjust the position of the gondola to ensure that CG is on the X_b or Z_b axis. After the gondola is ballasted

to neutral buoyancy, we add test weights on the gondola to create accurate and constant traction force with direction along Z_n axis. The test weights are pre-calibrated such that the total gravity is exactly one and two gram-force larger than the buoyancy for the movements along X_b and Z_b separately. The blimp is then released with zero velocity and the initial attitude of GT-MAB is demonstrated in Fig. 4. The experiments are conducted inside a laboratory with neglectable airflow perturbation. A total of 10 ceiling-mounted OptiTrack cameras capture the movement of the localization markers at the top of the envelope. The raw measurements from the motion tracking system are recorded and then converted to the position of the blimp in the inertial frame with the method discussed in Section III-A.

The experiments for the motion along X_b and Z_b axes are both repeated 21 times where the GT-MAB is released from different altitudes. Total flight duration is 152.73 seconds for the motion along X_b, and 143.88 seconds for the movement along Z_b. All flight data is captured at sampling rate of 120Hz. We use the first 20 datasets for parameter identification and reserve the last one for validation. The average estimate for the parameters in Eq. (22) are listed in Table I. The standard deviation of each identified parameter is approximately one magnitude smaller than the mean value. Fig. 5 demonstrates the close alignment between the validation data and the reconstructed response with the identified model. Given that m_{RB} was identified to be 0.1249kg in our previous works [18], [19], we get $m_{Ax} = 0.0466$kg, and $m_{Az} = 0.0545$kg.
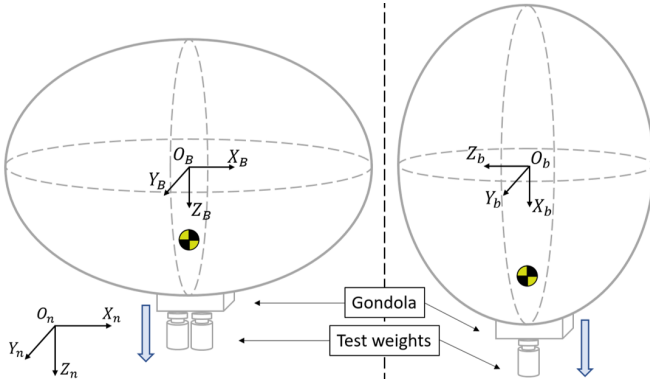

Fig. 4. Experimental setup for identifying the added mass and the drag coefficients for the motion along GT-MAB's body axes. The direction of the movement is annotated with blue arrow.

TABLE I

PARAMETERS IDENTIFIED FROM THE EXPERIMENTAL DATASETS

Parameter	Mean	Standard Deviation	Avg. NRMSE Fit
m_x	0.1715	0.0111	99.34%
D_{vx}^{CB}	0.0125	0.0019	
m_z	0.1794	0.0102	98.09%
D_{vz}^{CB}	0.0480	0.0037	

The parameters and the normalized root mean square error (NRMSE) are obtained from 20 datasets for the motion along X_b and Z_b separately.
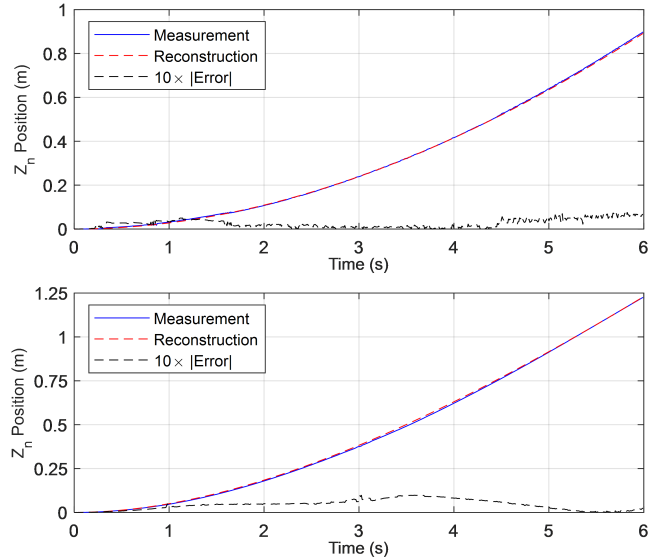

Fig. 5. Comparison between the validation data and the reconstructed response with identified model parameters. NRMSE fit is 98.61% for the motion along Z_b (upper), and 98.82% for the movement along X_b (lower). The magnitude of the error is enlarged 10 times for better illustration.

C. Parameters $r_{z,g/b}^b$, I_y, and $D_{\omega y}^{CB}$

Our previous works [18], [19] have identified the center-of-mass position, and the rotational inertia and damping coefficient at CG:

$$r_{z,g/b}^b = 0.09705\text{m}$$
$$I_y^{CG} = 0.005821\text{kg}\cdot\text{m}^2 \qquad (23)$$
$$D_{\omega y}^{CG} = 0.000980\text{N}\cdot\text{m}\cdot\text{s/rad}.$$

Thus, the rotational inertia at CB, I_y, can be derived from the parameters in Eq. (23). With system transformation matrix described in Eq. (8), we first represent the inertia at CG as:

$$M^{CG} = M_{RB}^{CG} + H^{-\top}(r_{g/b}^b)M_A^{CB}H^{-1}(r_{g/b}^b)$$
$$I_y^{CG} = m_{Ax}(r_{z,g/b}^b)^2 + I_{Ay} + I_{RBy}. \qquad (24)$$

From Eq. (9), we know that the rotational inertia at CB is:

$$I_y = I_y^{CB} = I_{RBy} + m_{RB}(r_{z,g/b}^b)^2 + I_{Ay}, \qquad (25)$$

Then, the parameter I_y can be calculated as:

$$I_y = I_y^{CG} - m_{Ax}(r_{z,g/b}^b)^2 + m_{RB}(r_{z,g/b}^b)^2$$
$$= 0.0066\text{kg}\cdot\text{m}^2. \qquad (26)$$

Similarly, $D_{\omega y}^{CB}$ can be found by representing the rotational aerodynamic damping coefficient at CG as:

$$D^{CG} = H^{-\top}(r_{g/b}^b)D^{CB}H^{-1}(r_{g/b}^b)$$
$$D_{\omega y}^{CG} = D_{\omega y}^{CB} + D_{vx}^{CB}(r_{z,g/b}^b)^2. \qquad (27)$$

Therefore, from the damping coefficient at CG in Eq. (23), we can find $D_{\omega y}^{CB} = 0.000862\text{N}\cdot\text{m}\cdot\text{s/rad}$.

IV. CONCLUSIONS AND FUTURE WORKS

This work establishes the motion model of the miniature indoor blimp, GT-MAB. The full model of this symmetrically-designed blimp is reduced to 3-DOF to simplify the representation and identification of the coupled translational and rotational movements. Parameters of the reduced motion model are identified and validated with experimental data.

We plan to design flight controllers to stabilize the swing oscillation while simultaneously keep the blimp cruising at the desired velocity. The modeling and controller design efforts will be extended to full 6-DOF. We will also explore data-driven methods that identify both structure and parameters of the motion model at the same time.

V. ACKNOWLEDGMENTS

REFERENCES

[1] S. Grzonka, G. Grisetti, and W. Burgard, "A fully autonomous indoor quadrotor," *IEEE Transactions on Robotics*, vol. 28, no. 1, pp. 90–100, 2012.

[2] S. Shen, N. Michael, and V. Kumar, "Autonomous multi-floor indoor navigation with a computationally constrained micro aerial vehicle," in *2011 IEEE International Conference on Robotics and Automation*, 2011, pp. 2968–2969.

[3] V. Mai, M. Kamel, M. Krebs, A. Schaffner, D. Meier, L. Paull, and R. Siegwart, "Local positioning system using uwb range measurements for an unmanned blimp," *IEEE Robotics and Automation Letters*, vol. 3, no. 4, pp. 2971–2978, 2018.

[4] D. Palossi, A. Gomez, S. Draskovic, A. Marongiu, L. Thiele, and L. Benini, "Extending the lifetime of nano-blimps via dynamic motor control," *Journal of Signal Processing Systems*, vol. 91, no. 3-4, pp. 339–361, 2018.

[5] K. Asadi, A. K. Suresh, A. Ender, S. Gotad, S. Maniyar, S. Anand, M. Noghabaei, K. Han, E. Lobaton, and T. Wu, "An integrated ugv-uav system for construction site data collection," *Automation in Construction*, vol. 112, p. 103068, 2020.

[6] S. U. Ferdous, A. Mohammadi, and S. Lakshmanan, "Developing a low-cost autonomous blimp with a reduced number of actuators," in *Unmanned Systems Technology XXI*, vol. 11021. SPIE, 2019, pp. 73 – 80.

[7] W. Yamada, H. Manabe, and D. Ikeda, "Zerone: Safety drone with blade-free propulsion," in *Proceedings of the 2019 CHI Conference on Human Factors in Computing Systems*, 2019.

[8] B. Siciliano and O. Khatib, *Springer handbook of robotics*. Germany: Springer-Verlag, 2016.

[9] "Crazyflie 2.1 product page," https://store.bitcraze.io/products/crazyflie-2-1, [Accessed: 23- May- 2020].

[10] F. Zhang, Q. Tao, T. Tan, P. Cheng, S. Cho, V. Mishra, and J. Varnell, "Miniature autonomous robotic blimp," U.S. Utility Patent App. 16/280,579, 20, 2019.

[11] N. Yao, Q. Tao, W. Liu, Z. Liu, Y. Tian, P. Wang, T. Li, and F. Zhang, "Autonomous flying blimp interaction with human in an indoor space," *Frontiers of Information Technology & Electronic Engineering*, vol. 20, no. 1, pp. 45–59, 2019.

[12] S. Cho, V. Mishra, Q. Tao, P. Varnell, M. King-Smith, A. Muni, W. Smallwood, and F. Zhang, "Autopilot design for a class of miniature autonomous blimps," in *Proc. of IEEE Conference on Control Technology and Applications (CCTA)*, 2017.

[13] Y. B. Sebbane, *Lighter than air robots*. Dordrecht, Netherlands: Springer, 2012.

[14] Q. Tao, M. King-Smith, A. Muni, V. Mishra, S. Cho, P. Varnell, and F. Zhang, "Control theory - autonomous blimp," in *IEEE CSS Video Clip Contest*, 2015.

[15] N. Yao, E. Anaya, Q. Tao, S. Cho, H. Zheng, and F. Zhang, "Monocular vision-based human following on miniature robotic blimp," in *IEEE International Conference on Robotics and Automation (ICRA)*, 2017.

[16] L. Seguin, J. Zheng, A. Li, Q. Tao, and F. Zhang, "A deep learning approach to localization for navigation on a miniature autonomous blimp," in *The 16 th IEEE International Conference on Control & Automation*, in press.

[17] J. Gibson, T. Schuler, L. McGuire, D. M. Lofaro, and D. Sofge, "Swarm and multi-agent time-based a* path planning for lta3 systems," *Unmanned Systems*, in press.

[18] Q. Tao, T. J. Tan, J. Cha, Y. Yuan, and F. Zhang, "Modeling and control of swing oscillation of underactuated indoor miniature autonomous blimps," *Unmanned Systems*, in press.

[19] Q. Tao, J. Cha, M. Hou, and F. Zhang, "Parameter identification of blimp dynamics through swinging motion," in *2018 15th International Conference on Control, Automation, Robotics and Vision (ICARCV)*, 2018, pp. 1186–1191.

[20] Z. Ashraf and M. A. Choudhry, "Dynamic modeling of the airship using analytical aerodynamic model," in *2009 International Conference on Emerging Technologies*, 2009, pp. 188–193.

[21] Y. Li, M. Nahon, and I. Sharf, "Airship dynamics modeling: A literature review," *Progress in Aerospace Sciences*, vol. 47, no. 3, pp. 217 – 239, 2011.

[22] D. Palossi, "Self-sustainability in nano unmanned aerial vehicles: A blimp case study," in *Proceedings of the Computing Frontiers Conference*, 2017.

[23] D. St-Onge, P. Brèches, I. Sharf, N. Reeves, I. Rekleitis, P. Abouza-khm, Y. Girdhar, A. Harmat, G. Dudek, and P. Giguère, "Control, localization and human interaction with an autonomous lighter-than-air performer," *Robotics and Autonomous Systems*, vol. 88, pp. 165 – 186, 2017.

[24] S. Kale, P. Joshi, and R. Pant, "A generic methodology for determination of drag coefficient of an aerostat envelope using cfd," *AIAA 5th ATIO and 16th Lighter-Than-Air Sys Tech. and Balloon Systems Conferences*, 2005.

[25] S. B. V. Gomes and J. G. Ramos, "Airship dynamic modeling for autonomous operation," in *Proceedings of IEEE International Conference on Robotics and Automation*, 1998.

[26] J. Shan, "Dynamic modeling and vision-based control for indoor airship," in *International Conference on Mechatronics and Automation*, 2009.

[27] J.-C. Zufferey, A. Guanella, A. Beyeler, and D. Floreano, "Flying over the reality gap: From simulated to real indoor airships," *Autonomous Robots*, vol. 21, no. 3, pp. 243–254, 2006.

[28] F. Hayato and S. Akira, "Wind-disturbance-based control approach for blimp robots," *Electronics and Communications in Japan*, vol. 97, no. 2, pp. 52–59, 2014.

[29] C. Wan, N. Kingry, and R. Dai, "Design and autonomous control of a solar-power blimp," in *2018 AIAA Guidance, Navigation, and Control Conference, AIAA SciTech Forum*, 2018.

[30] Y. Wang, G. Zheng, D. Efimov, and W. Perruquetti, "Altitude control for an indoor blimp robot," *IFAC-PapersOnLine*, vol. 50, no. 1, pp. 15 990 – 15 995, 2017, 20th IFAC World Congress.

[31] ——, "Disturbance compensation based controller for an indoor blimp robot," *Robotics and Autonomous Systems*, vol. 124, p. 103402, 2020.

[32] C. Blouin, E. Lanteigne, and W. Gueaieb, "Trajectory optimization of a small airship in a moving fluid," *Transactions of The Canadian Society for Mechanical Engineering*, vol. 40, pp. 191–200, 2016.

[33] V. Srisamosorn, N. Kuwahara, A. Yamashita, T. Ogata, S. Shirafuji, and J. Ota, "Indoor human face following with environmental fisheye cameras and blimp," *Advanced Robotics*, 2020.

[34] T. I. Fossen, *Handbook of Marine Craft Hydrodynamics and Motion Control*. United Kingdom: John Wiley & Sons, 2011.